

Orbital Structure of Collisionless Merger Remnants: On the Origin of Photometric and Kinematic Properties of Elliptical and S0 Galaxies

R. Jesseit^{1*}, T. Naab^{2†‡} and A. Burkert^{1§}

¹ *Universitätssternwarte, Scheinerstr. 1, 81679 München, Germany,*

² *Institute of Astronomy, Madingley Road, Cambridge, CB3 0HA, UK*

Submitted to MNRAS —; Accepted —

ABSTRACT

We present a detailed investigation of the relation between the orbital content of merger remnants and observable properties of elliptical and S0 galaxies. Our analysis is based on the statistical sample of collisionless mergers of disk galaxies with different mass ratios and orbital parameters, published by Naab & Burkert. We use the spectral method by Carpintero & Aguilar to determine the orbital content of every remnant and correlate it with its intrinsic shape, and its projected kinematic and photometric properties. We discuss the influence of the bulge component and varying pericenter distances. The classified orbit families are box orbits, minor axis tubes, inner and outer major axis tubes, and boxlets. In general, box orbits dominate the inner parts of the remnant. Major and minor axis tubes become dominant at intermediate radii and boxlets at large radii. The two most abundant orbit classes are the minor axis tubes and the box orbits. Their ratio seems to determine the basic properties of a remnant. On average, the fraction of minor axis tubes increases by a factor of two from a merger mass ratio of 1:1 to 4:1, whereas the fraction of box orbits decreases by 10%. At a given mass the central velocity dispersion of a remnant scales with the ratio of minor axis tubes to box orbits. Interestingly, the division line between rotational supported systems and pressure supported objects, $(v_{maj}/\sigma_0)^* = 0.7$, turns out to coincide with a box to minor axis tube ratio of unity. The observed h_3 - v/σ anti-correlation for ellipticals can not be reproduced by collisionless merger remnants. We propose that this can only be reconciled by an additional physical process that significantly reduces the box orbit content. Remnants which are dominated by minor axis tube orbits have predominantly disk projections. Boxy remnants have always a box to minor axis tube ratio larger than one. This study will enable to identify observed ellipticals that could have formed, in the collisionless limit, by gas-poor disk mergers. In addition, it demonstrates how observable properties of spheroidal stellar systems are connected with their intrinsic orbital structure.

Key words: stellar dynamics – orbital structure — galaxies: elliptical — galaxy formation.

1 INTRODUCTION

Elliptical galaxies show a richness of distinct substructure in their isophotal shape and velocity anisotropy. Bender (1988) and Bender, Döbereiner, & Möllenhoff (1988) found that elliptical galaxies can be divided into objects with

boxy and disk isophotal shape. Interestingly, ellipticals with boxy isophotes show X-ray emission in excess of discrete sources indicative of a hot gaseous halo, rotate slowly, and have higher luminosity while disk ellipticals are fast rotators, with low luminosities and no detectable X-ray halos Bender et al. (1989). These features are probably linked to the formation process of these galaxies. Toomre & Toomre (1972) were the first to propose that ellipticals could originate from mergers of two disk galaxies. Subsequent N-body simulations of collisions of disk galaxies showed that merger remnants mimic important features of elliptical galaxies like

* E-mail: jesseit@usm.uni-muenchen.de

† E-mail: naab@usm.uni-muenchen.de

‡ Present Address: Universitätssternwarte, Scheinerstr. 1, 81679 München, Germany

§ E-mail: burkert@usm.uni-muenchen.de

global kinematic and photometric properties, kinematic misalignments or kinematically decoupled cores (Barnes 1992, Hernquist 1992, Hernquist 1993, Heyl, Hernquist, & Spergel 1994, Heyl, Hernquist, & Spergel 1996, Weil & Hernquist 1996, Naab, Burkert, & Hernquist 1999, Bendo & Barnes 2000, Cretton, Naab, Rix, & Burkert 2001, Naab & Burkert 2003, Burkert & Naab 2004). Bender, Saglia, & Gerhard (1994) showed that the asymmetry of the line-of-sight-velocity-distribution (LOSVD), correlates with the ratio of local rotation velocity to velocity dispersion (v/σ). The LOSVD in general shows a steep leading wing. These findings have been confirmed by newer observations (Halliday et al. 2001, Pinkney et al. 2003).

If we consider ellipticals as pure stellar systems all kinematic and photometric properties will originate from the projected superposition of the orbits of individual stars, which build up the galaxy. Unfortunately, the trajectories of the stars themselves are not observable. Reliable constraints about the intrinsic shape can only be inferred statistically if a large sample of observed ellipticities is available like for the SDSS (Alam & Ryden 2002). To deproject an individual galaxy and determine its orbital content is much harder. The only tool available are Schwarzschild models (Schwarzschild 1979), where a library of orbits is fitted to the light distribution and, if available, to the detailed kinematics of a galaxy (see Rix et al. 1997 and references therein). One limitation is that most of these models assume that the fitted galaxy is intrinsically axisymmetric which might not always be the case in nature (Statler, Emsellem, Peletier, & Bacon 2004).

Simulated galaxies have the advantage that intrinsic and projected properties can be studied at the same time. Several authors investigated the orbital content of simulated merger remnants. One of the basic results was that the centre of the remnants is dominated by box orbits, while minor axis tubes dominate at larger radii (Barnes 1992). In agreement with theory they found that major axis tubes dominate in prolate remnants. The presence of gas in mergers has a significant impact on the orbital structure, as the box orbits at the centre are destroyed and minor axis tubes get more populated (Barnes & Hernquist 1996). Bendo & Barnes (2000) extracted the LOSVD for single orbit classes for a few merger remnants. Although these studies highlighted the importance of orbital structure and sometimes also discussed the effect of viewing angles (Heyl, Hernquist, & Spergel 1994, Heyl, Hernquist, & Spergel 1995), they were, however, limited to a small number of merger remnants.

Binney & Spergel (1982) originally proposed to use spectral dynamics for stellar dynamical problems. Laskar (1993) devised an algorithm to analyze dynamical spectra with high accuracy, which was also applied to analytical models of galactic systems (Papaphilippou & Laskar 1996; Papaphilippou & Laskar 1998). Carpintero & Aguilar (1998) (henceforth CA98) created a fully automated code to classify orbits in arbitrary two or three-dimensional potentials through spectral dynamics and which we will use in all our analysis presented in this paper. Whereas the orbital classification algorithms used for simulations so far picked up the different orbit families by checking if they change the sign of the angular momentum or not, the code of CA98 allows to distinguish orbit classes, which could not have been classified with simpler methods. The purpose of this paper is to identify the orbital content

of the merger remnants and connect it with their observable and intrinsic properties. The main ingredients are a large sample of collisionless merger remnants, software which mimics real life observations (Naab & Burkert 2003) and an orbit classification routine based on CA98. We study the orbit classes or superpositions of orbit classes, which are responsible for photometric properties, like isophotal shape and ellipticity, and kinematic properties of the remnants.

A brief introduction to the classification technique is outlined in Section 2. In Section 3 we explain the numerical tests and the merger remnants that are included in the sample. The following sections are concerned with global orbit abundance and radial distribution of orbit classes: Section 4 and section 5 describe the relation between the orbital content and intrinsic shape, Section 6 links photometric properties to the orbital structure. Kinematic properties are discussed in Section 7. Finally, we summarize and discuss the results in Section 8.

2 ORBIT CLASSIFICATION

Carpintero & Aguilar (1998) devised a code which automatically calculates the Fourier spectrum of the motion of a particle. It finds the most important resonances between the motions in x, y and z-direction, which are identified with long, intermediate and short axis of the potential the orbits are integrated in. We speak of a resonance when

$$l\omega_1 + m\omega_2 + n\omega_3 = 0 \quad (1)$$

for a non-trivial combination of integers l, m and n. Here $\omega_{i,i=1,2,3}$ denote the leading frequency in the direction of motion (in our case Cartesian coordinates). Every line in a spectrum of a 3-dimensional orbit can be expressed by a linear combination of up to three frequencies. These frequencies are also termed *fundamental frequencies*. If the code finds a fourth fundamental frequency the orbit is classified as *irregular*. Such an orbit has only one integral of motion, the energy.

Every orbit is analyzed at least twice, once with the full trajectory and once with some part removed. If this procedure results in two different classifications, then a third pass is made. However, if three different classifications are found then the orbit can not be classified. CA98 found very few cases in their analysis of analytical potentials, where this happened. We do find a low fraction of orbits (roughly 10%), which change their family during an integration and therefore fail to be assigned to an orbit class. Some loss seems to be inevitable in noisy N-body potentials. These orbits are termed *not classified*.

The resonances are the determining factor for the orbital classes and we divide the orbits up in five broad classes. The *minor axis tubes* have a 1:1 resonance of the motion in x and y-direction, or l=1, m=1 and n arbitrary. Similarly for the *inner major axis tube* and *outer major axis tube* classes, but with a 1:1 resonance of motion in the z and y-direction (m=1 and n=1). The code distinguishes these two orbit classes by a geometric, rather than spectral criterium: the inner major axis tubes are elongated and stay relatively close to the major axis, while the outer major axis tubes extend perpendicular to it and have a round shape. *boxlets* have either one or three resonances, barring a 1:1 resonance,

Table 1. Number of particles in merger remnants with different mass ratios

Mass Ratio	N_{lum}	N_{dark}
1:1	160000	240000
2:1	120000	180000
3:1	106666	160000
4:1	100000	150000

because then they would have a definite sense of rotation. For example, a 1:m:n=4:3:1 resonance would classify as a boxlet. The *box orbits* are the only orbit class which have no resonance.

The code was tested by CA98 on the singular, triaxial logarithmic potential, first analyzed by Schwarzschild (1993). They found a very good agreement between their spectral method and the much more time consuming investigation of the surfaces of section. For mathematical details on the calculation of the frequencies we refer to the paper of CA98.

There are several features of the method by CA98 which makes it attractive for use on N-Body systems: 1.) It can distinguish more orbit classes than if we would just check if the orbits change the sign of a component of their angular momentum. 2.) It has an inbuilt routine, which checks the geometric differences of inner and outer major axis tubes, which could otherwise not be identified by the spectral method. 3.) It corrects automatically for the center of the potential. 4.) Slight twists of the principal axes can be taken into account by the code, as long as the opening of a tube orbit is large enough, i.e. the orbit has a high angular momentum.

3 REMNANT SELECTION AND NUMERICAL TESTS.

3.1 Figure rotation

The statistical set of 112 merger simulations of disk galaxies with mass ratios of 1:1, 2:1, 3:1 and 4:1 is described in detail in Naab & Burkert (2003). Here we only give a brief summary. We used the following system of units: gravitational constant $G=1$, exponential scale length of the larger disk $h = 1$ and mass of the larger disk $M_d = 1$. Each galaxy consists of an exponential disk, a spherical, non-rotating bulge with mass $M_b = 1/3$, a Hernquist density profile (Hernquist 1990) with a scale length $r_b = 0.2h$ and a spherical pseudo-isothermal halo with a mass $M_d = 5.8$, cut-off radius $r_c = 10h$ and core radius $\gamma = 1h$. The equal-mass mergers were calculated adopting in total 400000 particles with each galaxy consisting of 20000 bulge particles, 60000 disk particles, and 120000 halo particles. The low-mass companion contained a fraction of $1/\eta$ the mass and the number of particles in each component with a disk scale length of $h = \sqrt{1/\eta}$, as expected from the Tully-Fisher relation (Pierce & Tully 1992). The galaxies approached each other on nearly parabolic orbits with an initial separation of $r_{sep} = 30$ length units and a pericenter distance of $r_p = 2$ length units. 16 different initial disk inclinations were selected in an unbiased way, following the procedure described by Barnes (1998).

In addition to the already published sample we simulated 16 1:1 merger remnants with an initial pericenter distance three times larger than in the original sample and 16 1:1 mergers with the original pericenter distance, but without bulges. We will discuss only the general properties of this control sample in Section 4.1

All simulations have been performed using the newly developed tree code VINE (Wetzstein, Nelson, Naab & Burkert, in prep.) in combination with GRAPE-5 (Kawai, Fukushige, Makino, & Taiji 2000). The Plummer-softening for the force calculation was set to $\epsilon = 0.05$. Time integration was performed with a Leap-Frog integrator with a fixed time-step of $\Delta t = 0.04$.

In this paper we restrict the orbit analysis to merger remnants without significant figure rotation. After the merger of the central parts of the galaxies was complete we allowed the remnants to settle into equilibrium for approximately 10 dynamical times (the half mass rotation period of the more massive progenitor disk). Thereafter we computed the amplitude and the phase of the $m = 2$ mode for 20 consecutive snapshots separated by 0.05 dynamical times. Remnants with phase differences larger than $\Delta\phi = 0.2$ are considered to have figure rotation and were removed from the sample. In total we excluded 18% of the 1:1, 12% of the 2:1, 15% 3:1 and 18% of the 4:1 remnants from the sample. The classification of orbits in rotating potentials requires additional care (Pfenniger & Friedli 1991) and will be discussed in a forthcoming paper.

3.2 Potential Reconstruction

To calculate the orbits of individual particles we fitted the potential of every merger remnant using a self-consistent field method (SCF, Hernquist & Ostriker 1992). With this method the Poisson equation is solved by expanding the potential and the density in a bi-orthogonal basis set $[\rho_{nlm}(r), \Phi_{nlm}(r)]$ as

$$\rho(r) = \sum_{nlm} A_{nlm} \rho_{nlm}(r) \quad (2)$$

and

$$\Phi(r) = \sum_{nlm} A_{nlm} \Phi_{nlm}(r), \quad (3)$$

where n denotes the number of radial expansion terms and l, m the angular terms. For more details and tests see Hozumi (1997) and Hozumi & Hernquist (1995). The code used in this paper was kindly provided by Shunsuke Hozumi. Two different sets of basis functions have been widely used in the literature, one proposed by Clutton-Brock (1973) and one by Hernquist & Ostriker (1992), henceforth CB and HO. The first one is based on the Plummer sphere, which has a constant density core and the second one on the Hernquist sphere (Hernquist 1990), which has a cuspy $\rho \propto r^{-1}$ core. For every basis set it is, however, important to choose the proper scale length to represent the potential of every individual merger remnant correctly. We kept the number of expansion terms fixed and match the center of the true N-body potential iteratively (by varying the scale length) with the potential calculated by the SCF code. We found that the forces for the HO basis set deviate more strongly in the center from the true forces than the ones calculated from the

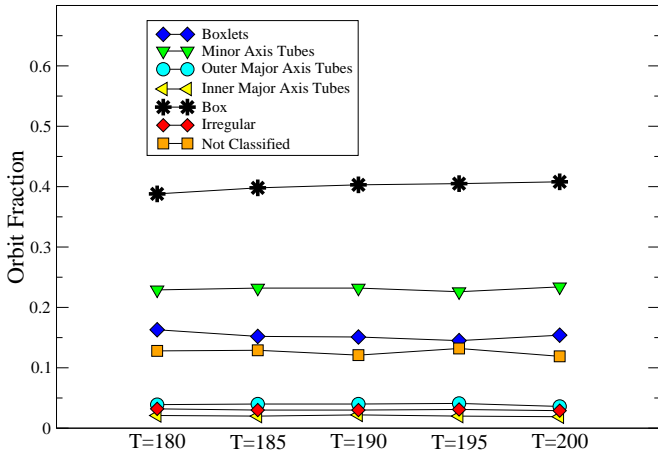


Figure 1. Time evolution of the classification results for a characteristic 1:1 merger remnant over ≈ 4 dynamical times. There is no significant evolution.

CB basis set. The merger remnants seem not to reach a high cuspidity, therefore the CB basis set was applied throughout this paper.

After the potential was reconstructed, we calculated the trajectories for all luminous particles using a high order Runge-Kutta integrator (Hairer, Nørsett & Wanner 1993) with automatic step size control. Every particle was integrated for approximately 30 dynamical times corresponding to ≈ 300 orbits in the central parts and ≈ 30 orbits around the effective radius of the remnant. All particles representing the luminous component were classified. The absolute numbers classified in each remnant are laid out in Table 1.

As a large number of angular expansion terms, high l , is only suitable for very flattened systems like disks, more radial terms than angular terms have been used. The same remnant was classified with $(n=12, l=6)$, $(n=12, l=4)$, $(n=8, l=6)$, $(n=8, l=4)$ and $(n=6, l=4)$. Table 2 shows that the results hardly depend on the number of expansion terms. Only the runs with $l=6$ seem to have a minor effect on the orbit fractions, as the number of not classified orbits and irregular orbits increases by a few percent. We decided to use a large number of radial terms, $n=12$, and a small number of angular terms $l=4$. This has the advantage of having an acceptable calculation time, while keeping a sufficient number of expansion terms.

3.3 Time Evolution Test

Naab & Burkert (2003) tested that the merger remnants do not change their shape for at least 10 dynamical times. It would also be important to know if the orbital content is changing or not. In Fig. 1 we show five snapshots of a typical 1:1 merger remnant which are each separated by five computational time units. This is approximately 4 dynamical times at the half mass radius. All other parameters are kept fix. No significant evolution of the orbital content can be observed. We therefore can safely use the snapshot at $t=200$ to analyze the internal structure of a merger remnant.

4 ORBITS IN MERGER REMNANTS

In this section we discuss the results of the orbit analysis applied to the sample of collisionless merger remnants. The abundance of different orbit classes in dependence of the adopted initial conditions, like mass ratio and impact parameter is highlighted. We examine the radial distribution of orbit classes inside a single merger remnant and trace the origin of different orbit classes back to the progenitor disk or bulge components.

4.1 General Results

To give an overview over the global orbit abundances we have determined the particle fraction of a given orbit class for the 40% most tightly bound stellar particles of every remnant which corresponds roughly to the region where global properties like the anisotropy parameter are observed. Fig. 2 shows the result, averaged over all remnants of a given mass ratio of the progenitor disks.

There are some clear trends connected to the mass ratio of the progenitors. The number of minor axis tubes is increasing with increasing mass ratio indicating that in unequal mass mergers it is more difficult to destroy the orbit population of the progenitor disks (see Naab & Burkert 2003). At the same time the boxlet and box orbit fractions decrease. Major axis tubes of both types only seem to be populated significantly in equal mass mergers. Over all there is only a small number of irregular orbits (less than 3%). The amount of not classified, class changing orbits is constant regardless of the mass ratio.

The influence of the impact parameter is shown in the bottom panel of Fig.2. For identical merger symmetries but with larger pericentral distance the minor axis tubes are populated more strongly than for the close encounter sample. Indeed it is now very difficult to form prolate remnants. Consequently, the amount of major axis tubes is much lower. Remnants from bulgeless progenitors show the opposite trend. They have much less minor axis tubes and many more box orbits of all types than the original sample with small pericenter distance. This confirms earlier findings that a central mass concentration tends to destroy the box orbits (Barnes & Hernquist 1996). The amount of irregular orbits is higher in the bulgeless remnants due to problems to fit the even shallower potentials with our basis sets.

4.2 Radial Distribution

The different orbit classes dominate at different radii inside the merger remnants. To show the radial dependence for individual objects, we plot four exemplary merger remnants in Fig.3: two 1:1 merger remnants, a 3:1 remnant and a remnant of bulgeless progenitors. Two 1:1 mergers have been chosen to demonstrate that different disk inclinations can lead to different orbital structure, while pericenter distance and mass ratio are identical. In the first three remnants the box orbits are most abundant at the center. Boxlets appear at all radii and start to dominate at large radii. This phenomenon has been found in various analytical potential models (see Lees & Schwarzschild, 1992 for details). The three tube orbit families start to dominate at intermediate radii, due to their non-zero angular momentum. In general,

Table 2. Classification results for a 1:1 merger remnant with different choices of expansion coefficients. The orbit fractions vary on the percent level. The runs with $l=6$ are slightly noisier and result in a somewhat higher number of not classified and irregular orbits.

(n,l)	Resonant Box	Minor Axis Tube	Outer Major Axis Tube	Inner Major Axis Tube	Box	Irregular	Not Classified
12,6	0.156	0.230	0.037	0.020	0.385	0.036	0.136
12,4	0.154	0.234	0.036	0.019	0.408	0.029	0.119
8,6	0.150	0.226	0.035	0.017	0.396	0.036	0.140
8,4	0.150	0.233	0.036	0.017	0.416	0.028	0.119
6,4	0.148	0.225	0.034	0.016	0.424	0.027	0.127

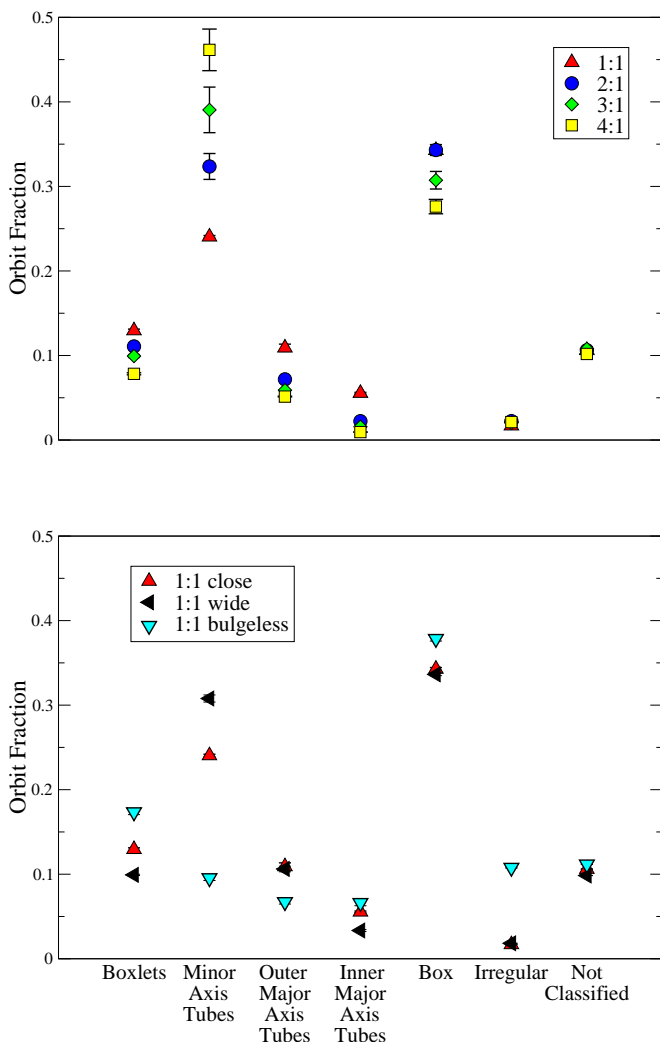


Figure 2. **Top:** Mean orbit fractions for the merger sample with small pericenter distance and different mass ratios. **Bottom:** Like before, but for equal mass mergers with small and big pericenter distance and without a bulge component

the mix of orbit classes is complicated, because the merger remnants do not have constant triaxiality with radius. Even the most prolate remnant, (second row, Fig. 3) has a significant amount of minor axis tubes. In a typical oblate remnant

only box orbits and minor axis tubes dominate. The bulgeless merger, however, is dominated at all radii by box orbits.

The radial distribution of orbit classes has been theoretically tested for a wide range of triaxial Stäckel models by Arnold, de Zeeuw, & Hunter (1994). The general trends they found agree well with the distributions in the merger remnants (compare with Fig.6 and Fig.8 of Arnold, de Zeeuw, & Hunter 1994)

4.3 Origin of Orbits from Disk or Bulge of Progenitors

The merging of two galaxies is a violent and randomizing process. It would be interesting to see whether certain orbit classes originate from the bulge component or the disk component of one of the progenitor galaxies. Fig.4 shows, averaged over all remnants with one mass ratio, which fraction of an orbit class originates from the massive disk, massive bulge, light disk and light bulge (which of course have the same mass in case of equal mass mergers). In the case of the 1:1 mergers we see that in one given orbit class an equal fraction originates from one of the two disks or from one of the two bulges. Particles originally in a bulge or a disk however populate different orbit classes. The most obvious trend is that minor axis tubes come mostly from the disk components and box orbits from the bulge component. Boxlets are slightly more likely to result from one of the disks, as do the outer major axis tubes.

With increasing mass ratio the minor axis tubes become more and more important. In the diagram for the 4:1 mergers it becomes clear that the overwhelming majority of the minor axis tubes were indeed part of the more massive disk. The contribution of massive disk and bulge to the box orbit population is remarkably independent of mass ratio.

5 ORBITS AND INTRINSIC SHAPE

The intrinsic shape of a triaxial mass distribution is defined by the ratio of its three principal axes. The principal axes are determined by diagonalising the moment of inertia tensor of each merger remnant. The particles are binned according to binding energy. That ensures that the subsets of particles follow the structure of the remnant naturally (Weil & Hernquist 1996). The triaxiality parameter T is defined as

$$T = \frac{1 - (b/a)^2}{1 - (c/a)^2}, \quad (4)$$

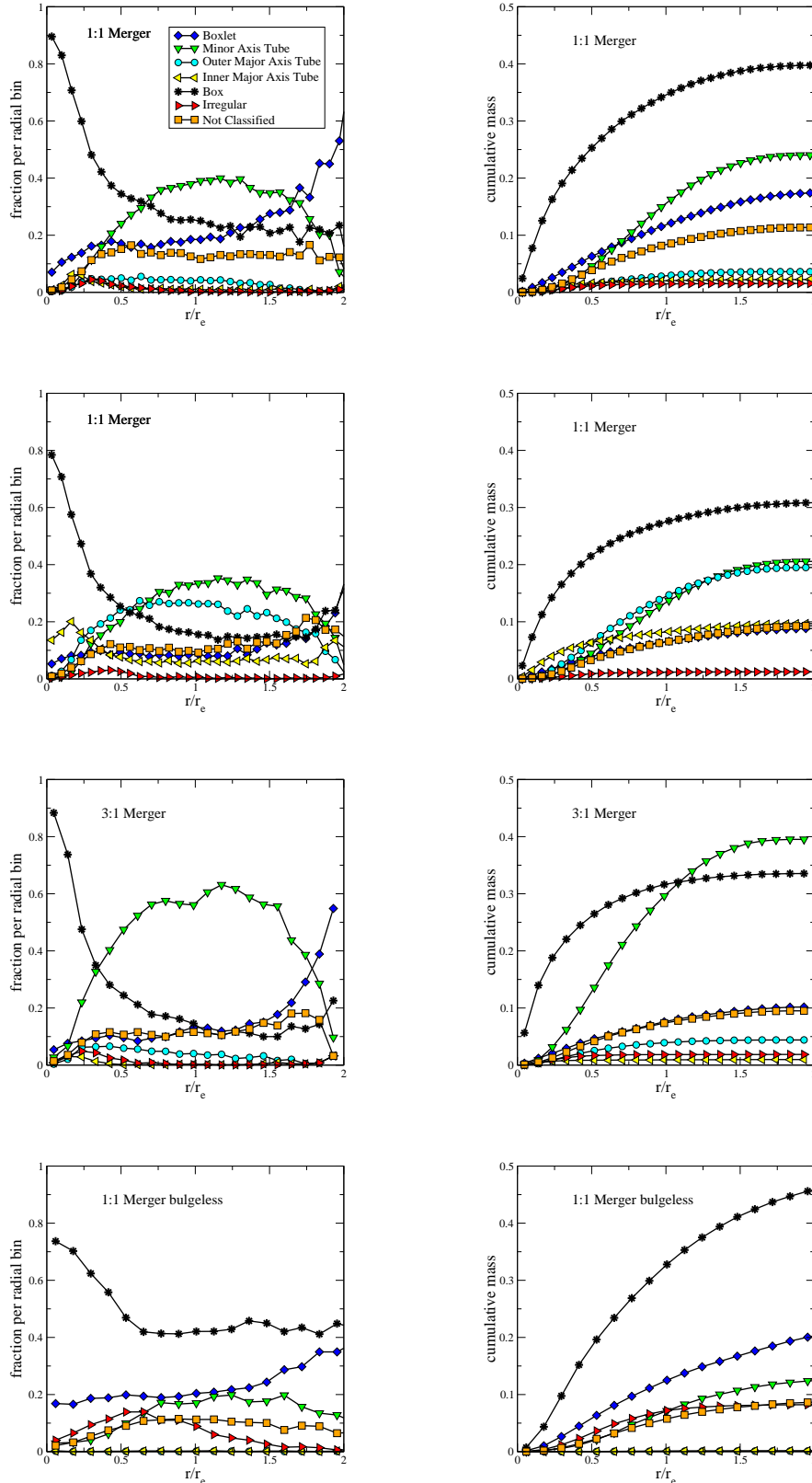


Figure 3. **Left Column:** Radial orbit distribution for different merger symmetries and mass ratios. The top two mergers are equal mass mergers from progenitors with different disk inclinations, but identical pericenter distance. Third row: 3:1 merger remnant. Bottom: Merger remnant of two equal mass bulgeless disks. **Right Column:** Cumulative mass profiles for the same merger remnants

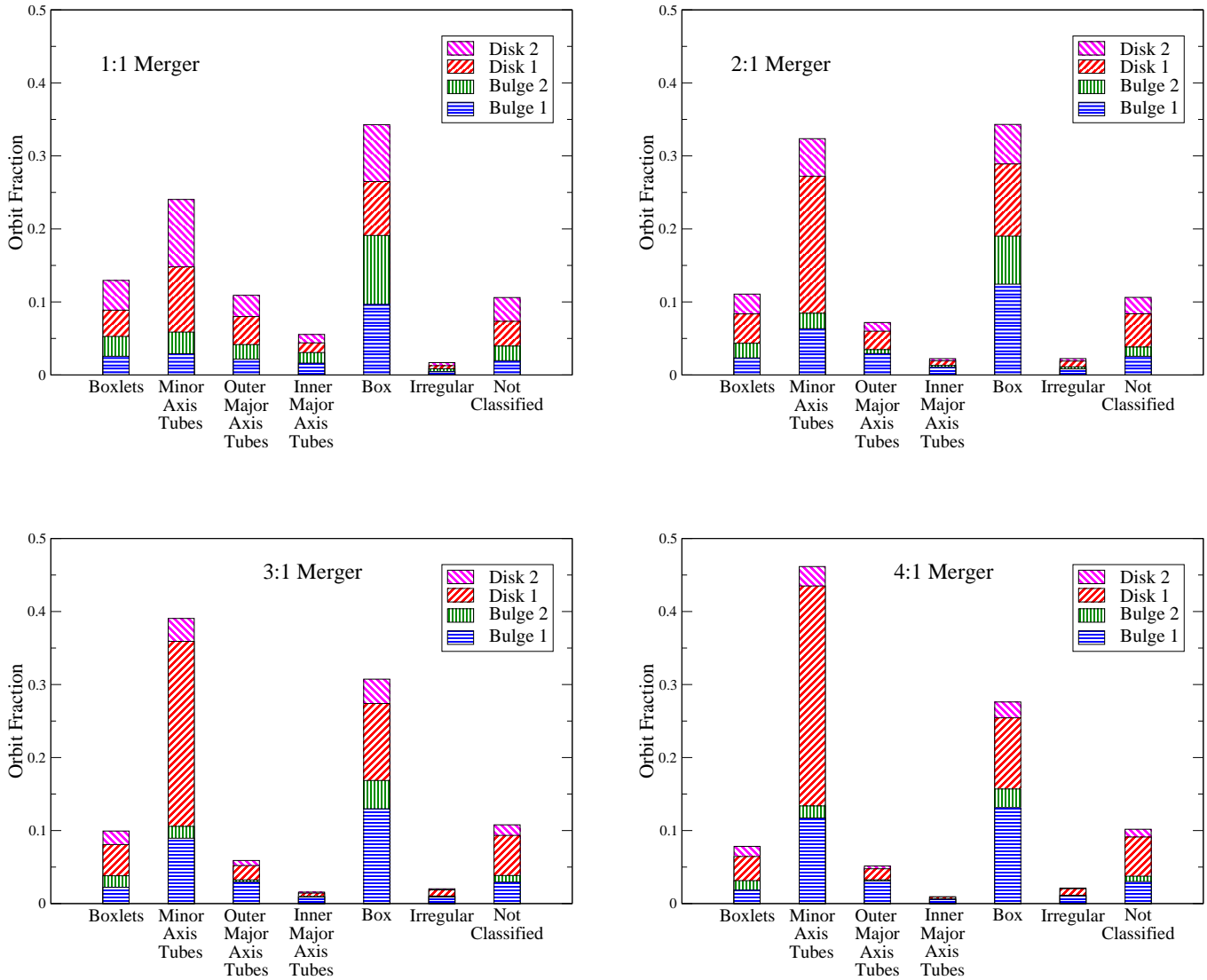


Figure 4. Origin of the orbit classes from the progenitor bulge or disk components. The histograms are shown for every mass ratio. The progenitor components denoted with a '1' come from the more massive merging partner in the case of unequal mass mergers.

where a , b , and c are the long, intermediate and minor axis, respectively.

In the following we used the 40% most bound particles to compute the triaxiality parameter. Fig.5 shows the distribution of the triaxiality parameter for the two most important orbit classes: the minor axis tubes and the box orbits. The minor axis tube fraction rises strongly with decreasing T to 60% for oblate shapes ($T = 0$) and drops to values as low as 20% for very prolate shapes ($T = 1$). The box orbit distribution peaks at $T = 0.5$, i.e. at maximum triaxiality, with a maximum value of around 40%. The box orbits depopulate quickly towards the prolate and oblate limits of the triaxiality parameter.

There is a considerable spread in the results, which in part can be explained, when we look at the two-dimensional probability density of the merger remnants in axis ratio space (Fig. 6). The same triaxiality can be achieved by dif-

ferent combinations of c/a and b/a . The spread in the correlation would be small if the probability contours would follow the lines of equal triaxiality. This is almost the case for the minor axis tubes. They are most abundant in very oblate remnants and depopulate very quickly for other shapes. The upper right panel of Fig. 6, which shows the box orbit abundance, the peak is located at $T = 0.5$. The probability contours are not parallel to the lines of constant triaxiality, but also have a gradient along the lines. The abundance of box orbits and minor axis tubes is almost anti-correlated. Those two families are the most dominant families in most of the remnants. This suggests that many kinematical features might depend on the ratio of the population of those two orbit families. We will explore the implications in the following sections.

Outer major axis tubes and inner major axis tubes are not occupying exactly the same positions in the diagrams.

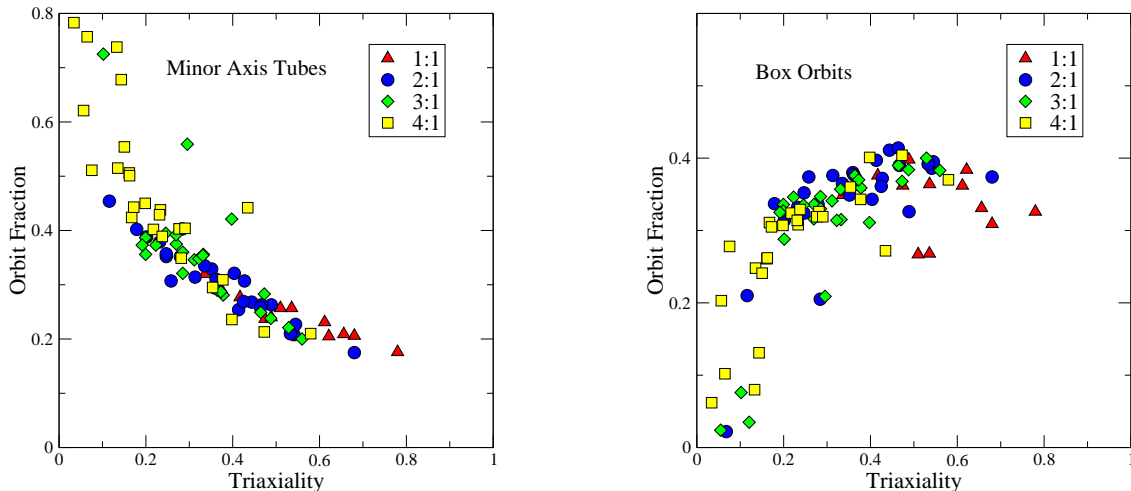


Figure 5. **Left:** Relation between the triaxiality parameter and the minor axis tube fraction. **Right:** Like before, but this time for the box orbit fraction.

Inner major axis tubes are abundant in more prolate models, while the outer major axis tubes are also common in remnants which tend to the spherical limit (the upper right corner in the axis ratio plot). This is the result of the shape of these orbit classes: the inner major axis tubes are more elongated along the major axis while outer major axis tubes support a round and thick shape.

6 ORBITS AND PHOTOMETRIC PROPERTIES

6.1 Orbital Shapes

As the remnants deviate significantly from axisymmetry, we have to consider the general case of orbits in triaxial potentials, when investigating the orbital shapes of individual orbit classes, e.g. orbit classes which exist in axisymmetric systems like the minor axis tubes, change their appearance in triaxial systems. This is illustrated qualitatively in Fig. 7, where for the five most important orbit classes exemplary trajectories are plotted projected onto the three principal planes (XY, XZ, and YZ). The projection of the minor axis tube (top row, Fig. 7) along the short axis appears round and has a hole in the center. Particles moving on such an orbit do not come close to the center because of their non vanishing in z-direction. The projection along the intermediate axis is flattened and disk-like, almost like one would expect in an axisymmetric system. However, the projection along the major axis is slightly peanut-shaped. That might imply that minor axis tubes do not contribute to disk-like isophotes for viewing angles close to this projection. The box orbits appear box shaped, with the exception of the projection along the major axis, where we look end on and the box orbits (second row) do not extend much. The outer and inner major axis tubes (row three and four) appear round along the major axis projection. The other two projections differ between both orbit classes. While inner major axis tubes have an elongated shape along the major

axis, the outer major axis tubes extend perpendicular to it and in general appear more round. The boxlets (last row) are resonant box orbits which have the same general features as their non-resonant brethren, but extend to larger radii. The orbits shown in Fig. 7 highlight how the photometric properties of the merger remnants might be influenced in a very complicated way by the superposition of different orbit classes as well as by the viewing angle. Empirically we find that the projections along the principal axes define the boundaries of the photometric properties, like ellipticity and isophotal shape. Therefore we focus on those projections in the following.

6.2 Ellipticity

We want to answer the question if the ellipticity is a good indicator of the intrinsic shape and the true orbital content. Observationally, the projected ellipticity has to be used to infer statistically the intrinsic shape distribution of real elliptical galaxies. In principle we have the advantage to know both the intrinsic and projected properties, but we defer a detailed analysis to a future paper. Instead we simply correlate the average, effective ellipticity, as defined in Naab & Burkert (2003), over fifty projections for every remnant with the box to minor axis tube ratio (Fig. 8). We see no obvious relation between the box to minor axis tube ratio and the mean ellipticity. To investigate the influence of the averaging process, we examine radial ellipticity profiles for individual galaxies, while keeping the viewing angle fixed. The radial ellipticity profiles of the XY-projection of the 1:1 and 2:1 remnants are shown in Fig. 9, top left. The shape is similar in each case: after a short initial rise the curves peak and then drop to low ellipticities. There is a trend, that peaks with higher ellipticity are located at larger radii. The value of the peak ellipticity correlates nicely with the box to minor axis tube ratio (Fig. 9, bottom left). This behaviour becomes clear if we remind ourselves that we superpose for this projection round tubes with elongated boxes (left most

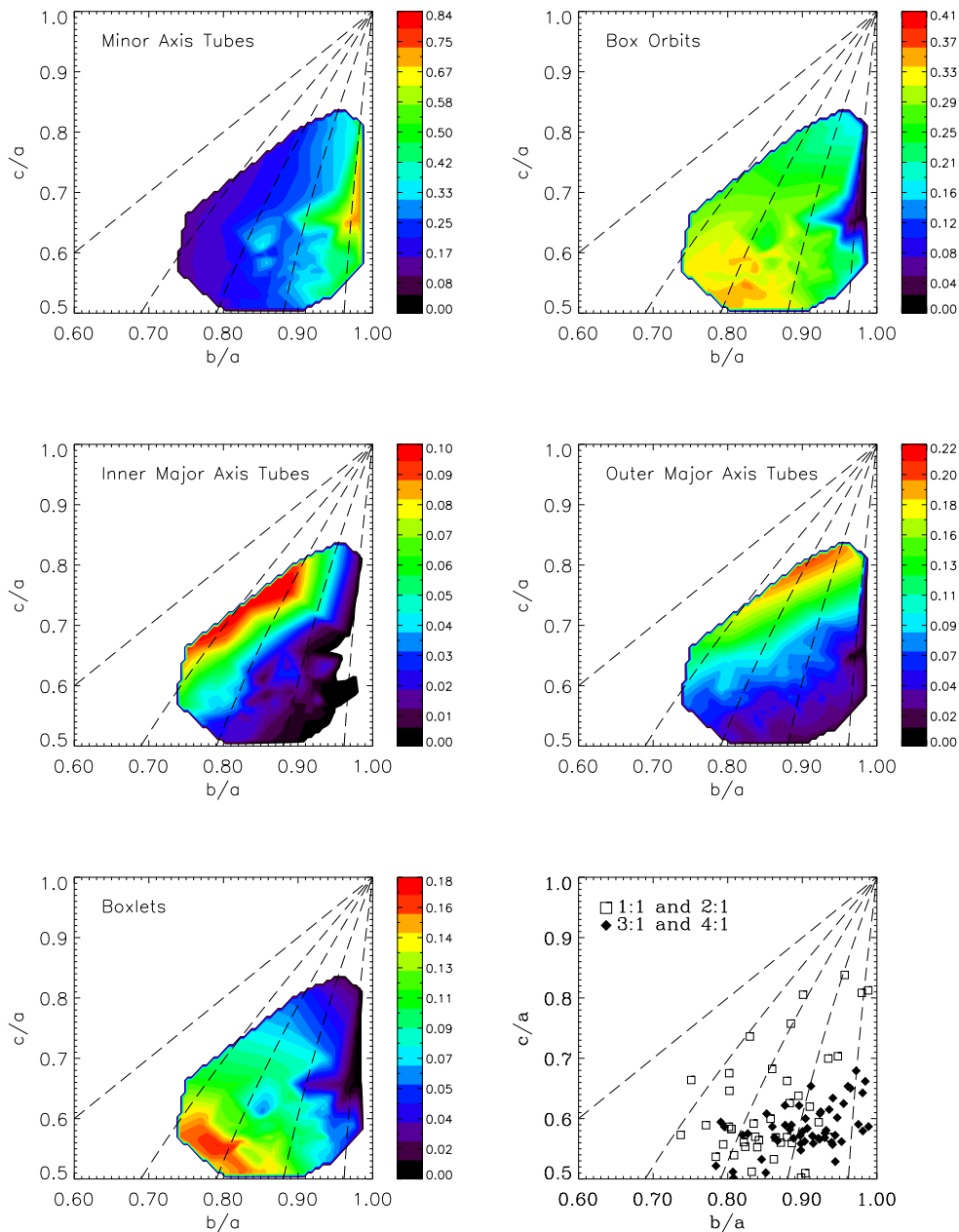


Figure 6. Color coded orbit abundances in axis-ratio space, where red designates the maximum abundance reached by a given orbit class for all remnants and black the minimum. a , b and c denote the long, intermediate and short axis of the 40% most bound particles of the remnants. Lines of equal triaxiality are over plotted. From left to right: $T=1, 0.7, 0.5, 0.3$. **Top left:** Minor axis tubes. **Top Right:** Box orbits. **Center Left:** Inner Major Axis Tubes. **Center Right:** Outer Major Axis Tubes. **Bottom Left:** Boxlets. **Bottom Right:** Location of merger remnants in the axis ratio diagram on which the abundances were interpolated

panels of the top two rows, Fig. 7). Only a significant fraction of box orbits can lead to an elongated appearance. In the outer parts, where the minor axis tubes dominate, the remnant appears round. The effect vanishes for 3:1 and 4:1 remnants, because their box orbit fraction is too low. Ellipticity profiles like this are not characteristic for early-type galaxies in general, but individual examples do exist.

The ellipticity profiles for the edge-on projections, e.g. onto the XZ-plane, first rise steeply and then flatten out to

larger radii. In Fig. 9, top right panel, we plot the ellipticity profiles for all 1:1 and 2:1 merger remnants. Most of them show the described behaviour, but some of them stay at remarkably low ellipticities. This time we do not find any correlation with the box or minor axis tube fractions. Instead the ellipticity of the edge on projection is very sensible to the fraction of outer major axis tubes, as indicated in Fig. 9, bottom right panel. Both minor-axis tubes and box orbits populations do not extend very much in the z-direction,

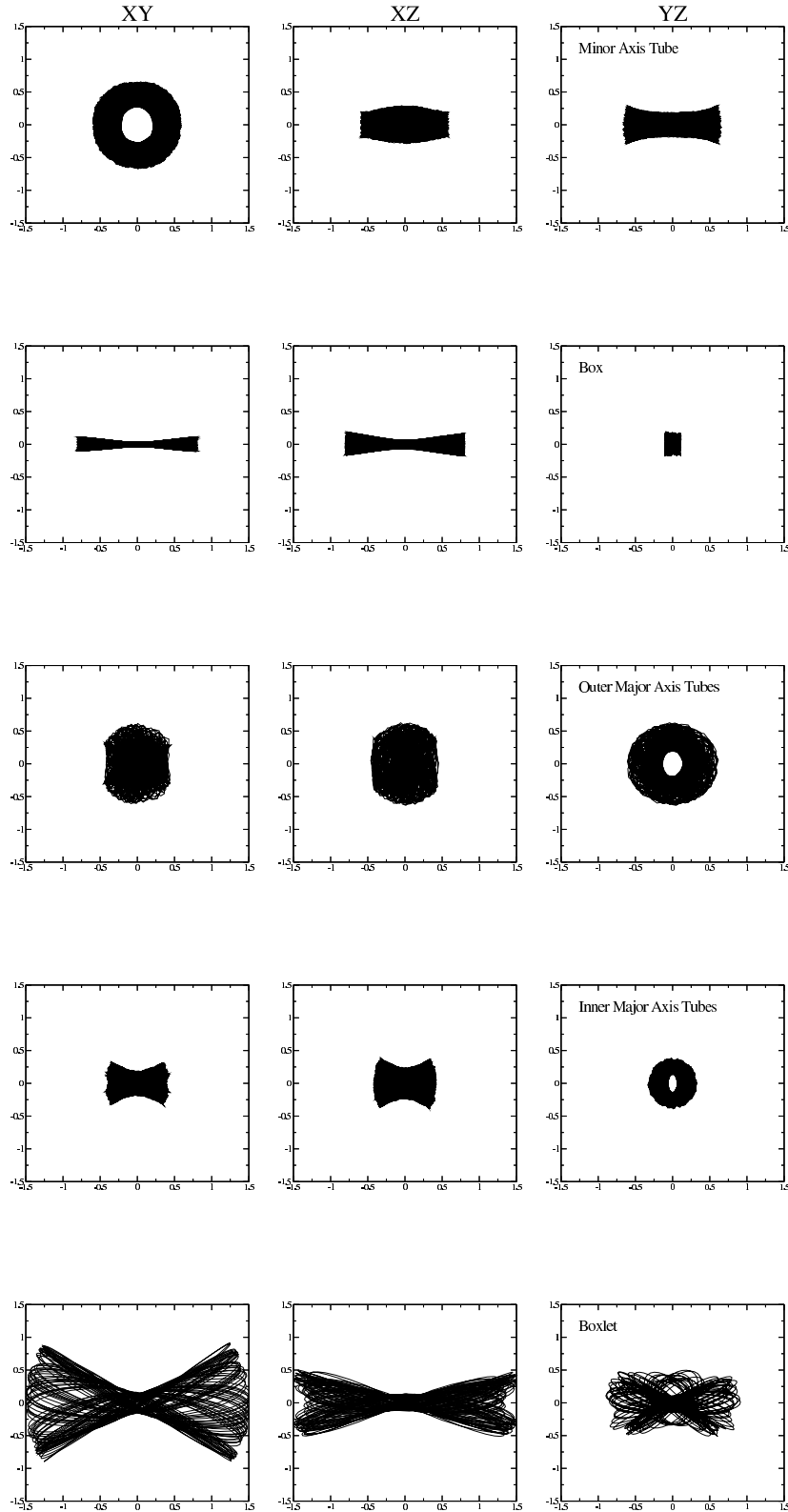


Figure 7. Orbits integrated in the potential of a 1:1 merger. This shows that the projection on the three symmetry planes can differ strongly for a given orbit class. Photometric properties change accordingly. **From top to bottom:** minor axis tube, box orbit, outer major axis tube, inner major axis tube and boxlet. **From left to right:** projection along the short axis (XY), along the intermediate axis (XZ) and along the major axis (YZ)

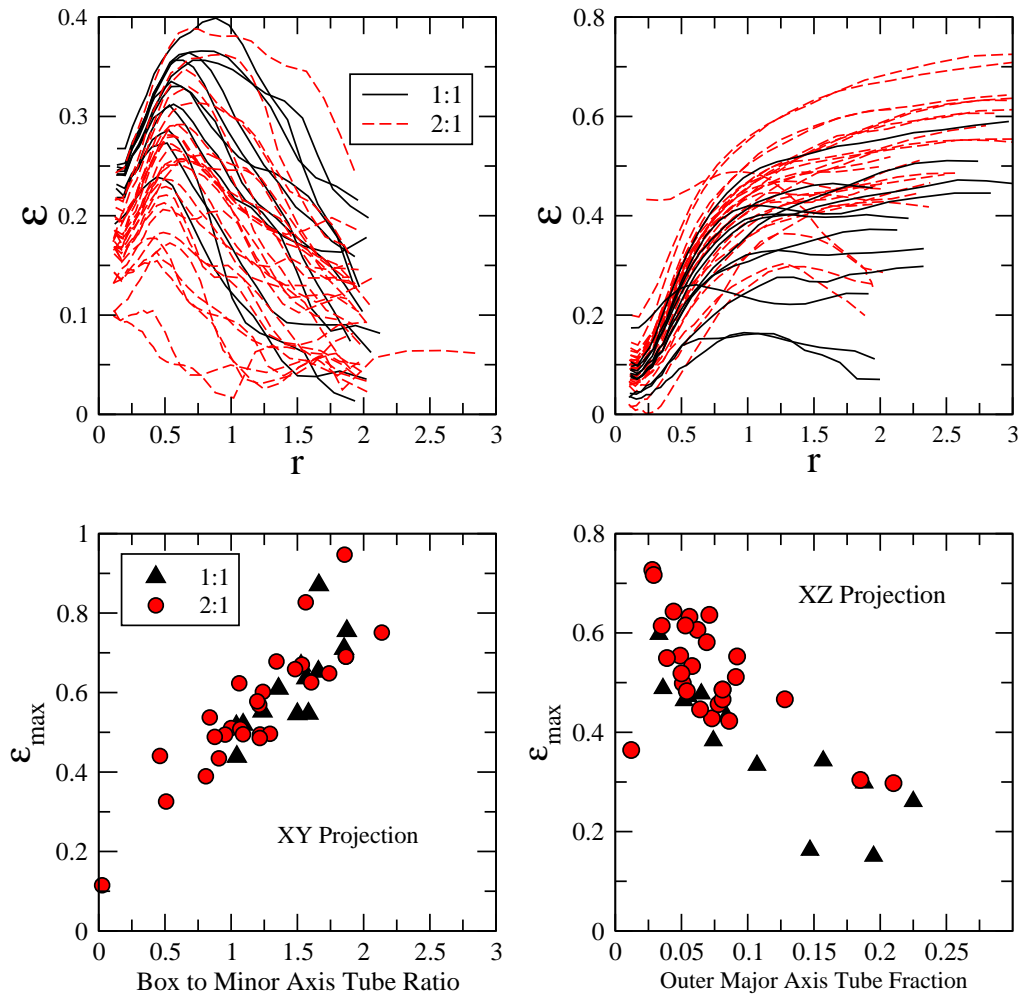


Figure 9. **Top Left:** Radial ellipticity profiles from the projection on the XY-plane of 1:1 and 2:1 merger remnants. **Top Right:** Radial ellipticity profiles from the projection on the XZ-plane of the same merger remnants. **Bottom left:** Relation between box to minor axis tube ratio and maximum ellipticity of the XY projection. **Bottom Right:** Relation between the outer major axis tube fraction and the maximum ellipticity of the XZ-plane.

only the outer major axis tubes do. Even a small fraction of major axis tubes seems to be able to lower the ellipticity significantly, i.e. make the shape rounder (see right most panels of the upper three rows in Fig. 7). The ellipticity of the 3:1 and 4:1 remnants seems to be determined by minor axis tubes alone.

6.3 Mean Isophotal Shape

Fig. 10 summarizes our results for the effective isophotal shape parameter a_4 , averaged over 50 projections, as defined in Naab & Burkert (2003). For a better discussion we partitioned the plot into four quadrants. The bottom right quadrant contains boxy remnants with a box to minor axis tube fraction larger than one. Only mergers of the 1:1 and 2:1 fraction can be found here. The opposite quadrant (top left) has disk-like remnants with a dominant minor axis tube population and contains no 1:1 mergers. Finally the bottom left quadrant (boxy and dominant minor axis tubes) has no

mergers, while in the upper right one (disk-like and dominant box orbits) every mass ratio can be found. The upper right quadrant is difficult to interpret. A dependence on the mass fraction can clearly be seen, but on the box to minor axis tube ratio not, at least for 3:1 and 4:1 mergers.

6.4 Viewing Angle and Isophotal Shape

Franx (1988) suggested that whether the isophotal shape appears disk-like or boxy depends not only on the intrinsic structure of the galaxy, but also on the viewing angle. This was confirmed in simulations of collisionless disk-disk mergers by Heyl, Hernquist, & Spergel (1994). As both, the intrinsic structure and the viewing angle are known for the merger remnants it is straight forward to combine this knowledge. The result is shown in Fig. 11. To study the influence of the viewing angle we examine only the projections along the principal axes of the merger remnants, which in almost all cases result in the most extreme values for a_4 and ϵ of all

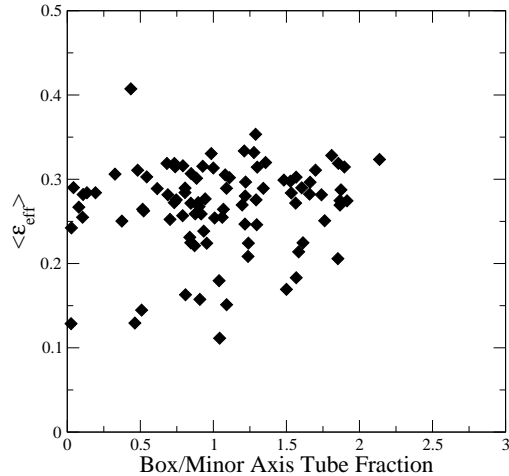


Figure 8. Relation between mean effective ellipticity and the box to minor axis tube ratio. The mean values lie between 0.1 and 0.3. There is no obvious connection between the intrinsic structure and the mean ellipticity

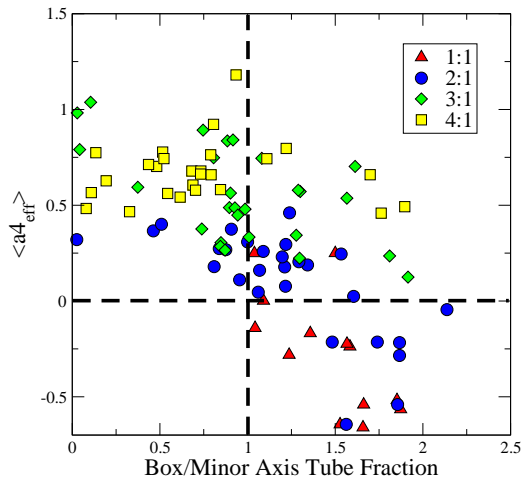


Figure 10. Relation between the box to minor axis tube ratio and the effective isophotal shape parameter. The vertical dashed line divides the box dominated from the minor axis tube dominated merger remnants. The horizontal line divides the separates the boxy remnants from the disky remnants.

possible projections. The projection along the major axis is the most sensitive to the orbital content of the merger remnants. In the top row of Fig. 11, we see that the remnants with negative a_4 indeed have a dominant box orbit population, while the most disky ones are dominated by minor axis tubes. Interestingly the remnants which have low ellipticities have the highest fraction of outer major axis tubes. The projection along the intermediate axis (second row) is the most complicated one. Almost none of the remnants are identified as boxy. Although most of the box orbits dominated remnants now lie close to the $a_4 = 0$ line, some have very disky projections. Finally the projection along the short

axis again is more sensible to the orbital content. The box orbit dominated remnants are boxy and the disky remnants are minor axis tube dominated.

Intrinsically the minor axis tubes lead to the most disky shape for short axis projections, while for the projection along the major axis their shape appears boxy or peanut-like. It seems that a small amount of minor axis tubes can counter the influence of the box orbits, but only for projections along or close to the intermediate axis. This is still enough to generate a large spread in the mean isophotal shape as a function of box-to-minor axis tube fraction (Fig. 10) for the 3:1 and 4:1 remnants.

7 ORBITS AND KINEMATIC PROPERTIES

The combination of all stars moving on different orbits defines the kinematic properties of the remnants. Different orbit classes, however, have different kinematical properties. Minor axis tubes are responsible for major axis rotation, while major axis tubes are minor axis rotators. Boxes and boxlets should have a vanishing mean angular momentum. This should result in correlations between the general kinematical properties of the remnants and their orbital content. To disentangle these relationships we have extracted the different orbit classes and analyzed their properties in isolation. This will help us to understand, global projected kinematic properties as well as more complex phenomena like the line-of-sight velocity distribution (LOSVD).

7.1 Rotational Support versus Pressure Support

The anisotropy parameter $(v_{maj}/\sigma_0)^*$ is defined as the ratio of the observed value of the rotation along the major axis and the central velocity dispersion, v_{maj}/σ_0 , and the theoretical value for an isotropic oblate rotator $(v/\sigma)_{theo} = [\epsilon_{obs}/(1 - \epsilon_{obs})]^{1/2}$ with the observed ellipticity ϵ_{obs} (Binney 1978). This parameter has been used by observers to determine whether a given galaxy is flattened by rotation $[(v_{maj}/\sigma_0)^* \geq 0.7]$ or by velocity anisotropy $[(v_{maj}/\sigma_0)^* < 0.7]$ (Davies et al. 1983, Bender 1988, Nieto, Capaccioli, & Held 1988, Scorza & Bender 1995). An intrinsic property of the two most abundant orbit classes is that the minor axis tubes are dynamically colder and have higher rotational velocities than the box orbits which generate no net rotation and which lead to high velocity dispersions. The relative abundance of these orbit classes is connected with the value of the anisotropy parameter as can be seen in Fig. 12. Interestingly all remnants with $[(v_{maj}/\sigma_0)^* > 0.7]$ are dominated by tube orbits while the majority of anisotropic remnants are box orbit dominated. The division line between isotropic and anisotropic remnants seems to coincide with a box to tube ratio of unity.

It is also instructive to examine the relation between velocity dispersion and major axis rotation directly. The Faber-Jackson relation (Faber & Jackson 1976) tells us that the central velocity dispersion in early type galaxies is tightly connected with the total luminosity (or mass) of the galaxy. In our sample the merger remnants have four different masses. Equal mass mergers have a total mass of twice the more massive progenitor, 4:1 mergers have a total mass of 1.25 the more massive progenitor or 62.5% the mass of

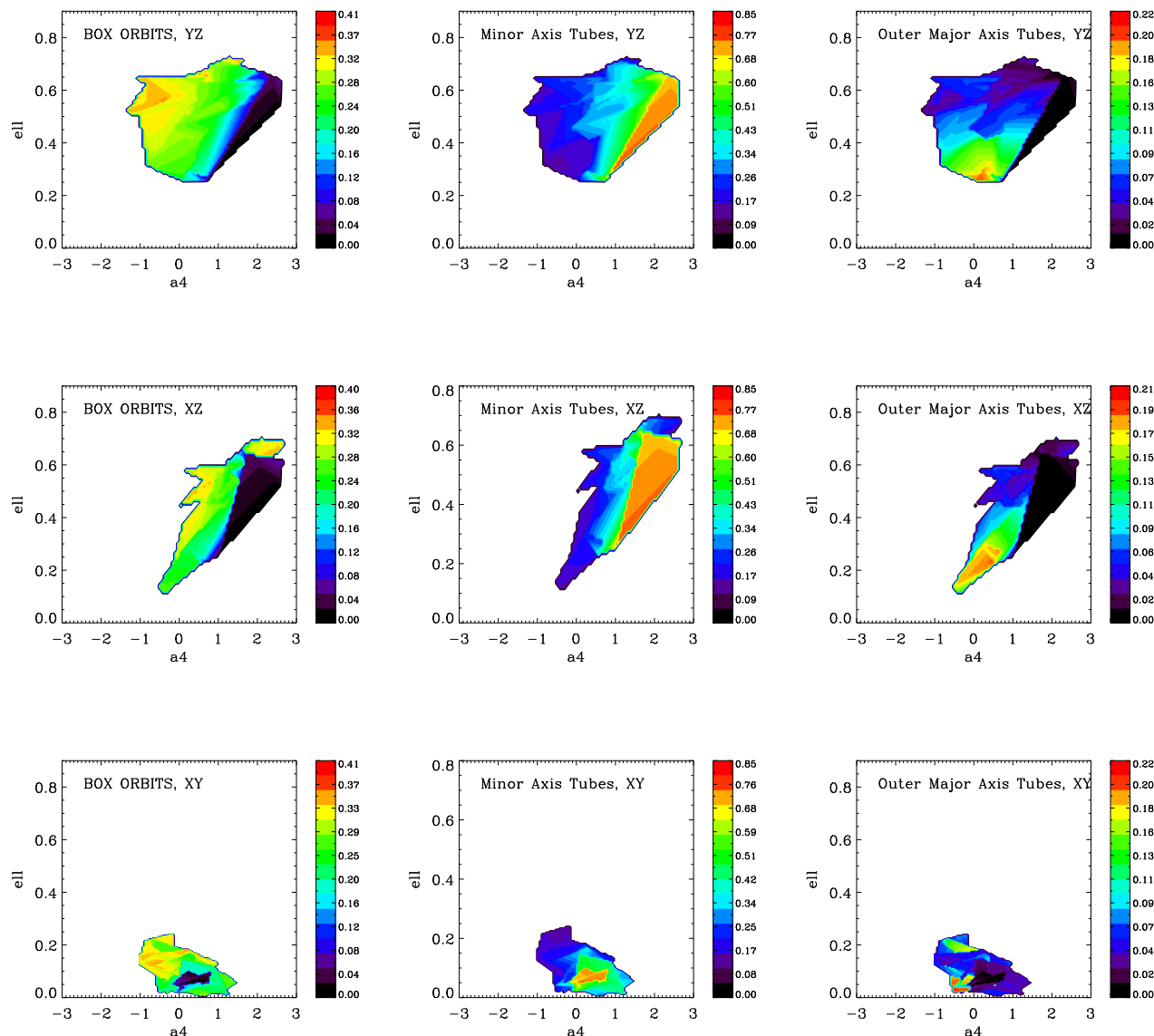


Figure 11. Relation between the photometric properties of the merger remnants, their intrinsic structure and the viewing angle. Color-coded orbit abundances are shown in the a_4 - ϵ plane. In each row we show from left to right the relation the abundance of box orbits, minor axis tubes and outer major axis tubes. **Top Row:** Projection along the major axis. For this projection the isophotal shape parameter shows the best correlation with the intrinsic structure. **Middle Row:** Projection along the intermediate axis. This is the most disk-like projection. The minor axis tube component can mask the influence of the box orbits effectively. **Bottom Row:** Projection along the short axis. All remnants have low ellipticities.

1:1 mergers. In Fig. 13 we plot the maximum projected central velocity dispersion of each remnant versus the box to minor axis tube ratio. The central velocity dispersion σ_0 of every remnant was determined as the average projected velocity dispersion of the luminous particles inside a projected galactocentric distance of $0.2 r_{\text{eff}}$. As expected more massive remnants have higher central velocity dispersions. What is more remarkable is that, for a given mass, there exists a correlation with the box to minor axis tube ratio. The conclusion must be that the central velocity dispersion is also an

indicator of initial conditions (in this case merging symmetry), which populate the different orbit classes accordingly. Unfortunately, if projection effects are taken into account, the correlation becomes less clear. It is hard to think of a way to use this property in observations of real ellipticals.

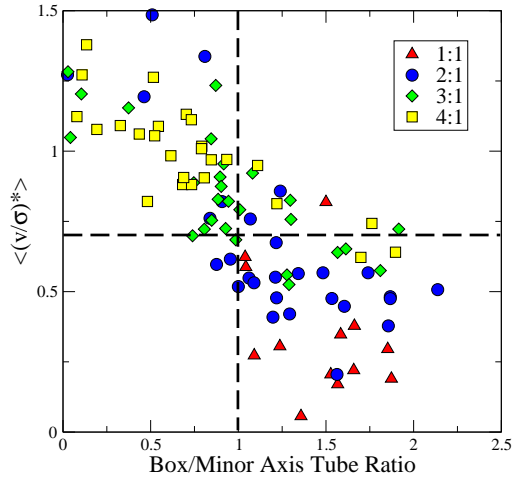


Figure 12. Relation between the anisotropy parameter $\langle (v/\sigma)^* \rangle$ and the box to minor axis tube ratio. The anisotropy parameter is averaged over 50 projections. The horizontal dashed line indicates $\langle (v/\sigma)^* \rangle = 0.7$ above which the system is expected to be flattened by rotation.

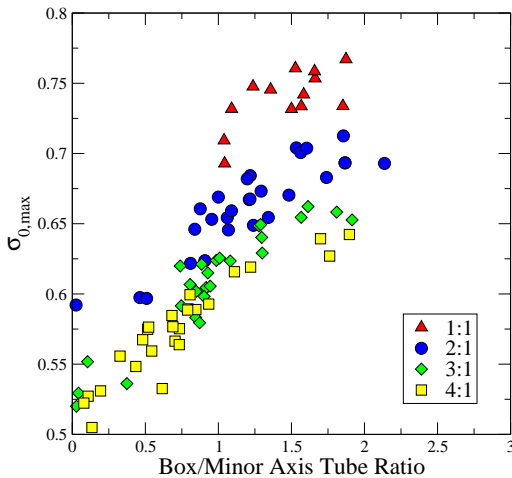


Figure 13. Relation between the maximum central velocity dispersion and box to minor axis tube ratio. The projection under which the maximum of the central velocity dispersion is found is exactly on or very close to the intermediate axis

7.2 Minor Axis Rotation

The amount of minor-axis rotation can be parameterized as $\mu = v_{\min}/(v_{\text{maj}}^2 + v_{\min}^2)^{1/2}$ (Binney 1985). It is an important indicator in combination with the isophotal twist for triaxiality in elliptical galaxies (Wagner, Bender, & Moellenhoff 1988, Franx, Illingworth, & de Zeeuw 1991). Only the 1:1 and 2:1 merger remnants have significant minor axis rotation (see also Fig. 13 of Naab & Burkert 2003). In Fig. 14 we plot μ versus the outer major axis tube fraction. μ is measured at $0.5r_{\text{eff}}$ and averaged over 50 projections. In general,

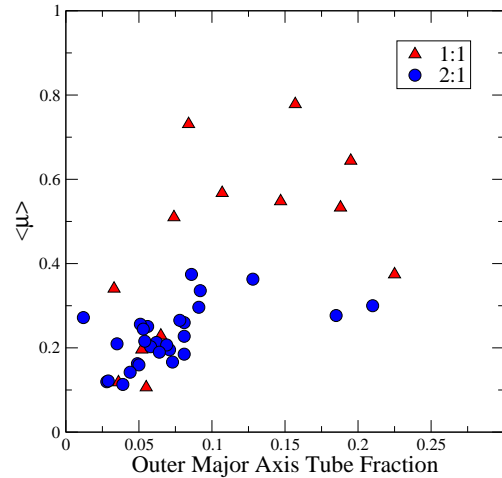


Figure 14. Relation between $\mu = v_{\min}/(v_{\text{maj}}^2 + v_{\min}^2)^{1/2}$ averaged over 50 projections and the outer major axis tube fraction. The μ -parameter is used in observational analysis to determine the amount of minor axis rotation in a galaxy.

mergers with a higher outer major axis tube fraction have a higher value of μ . Although this result is encouraging, there are some outliers with low minor axis rotation, but high outer major axis tube fraction. This could be explained by counter-rotating populations, which lower the minor axis rotation.

7.3 Line-of-Sight Velocity Distributions

7.3.1 Velocity Profiles

A simple test can show whether the particles which we have assigned to a certain orbit class show the typical kinematical behaviour that we would expect. In Fig. 15 the mean line-of-sight velocity (LOS v), along the three principal axes is shown. The measurement of the total merger remnant is compared with the signature which one would get by just analyzing the subset of particles, classified as minor axis tubes, major axis tubes and box orbits. The minor axis tubes show a higher rotation velocity for the two projections along the intermediate and the long axis (XZ and YZ) than the total remnant and show no rotation for the face on (XY) projection. Similarly in the same figure, second row, the major axis tubes show significant rotation for the XZ and the XY projection and almost no rotation for the YZ projection where we observe this orbit class face on. Note that the XZ projection has contributions from both tube types, the major and the minor axis tubes. This is the reason, why the major axis tubes dominate more for the XY projections, where there is no contribution from the minor axis tubes. Finally the box orbit population in a 3:1 remnant does not show any rotation, as we would expect, although the total remnant has a high amount of rotation.

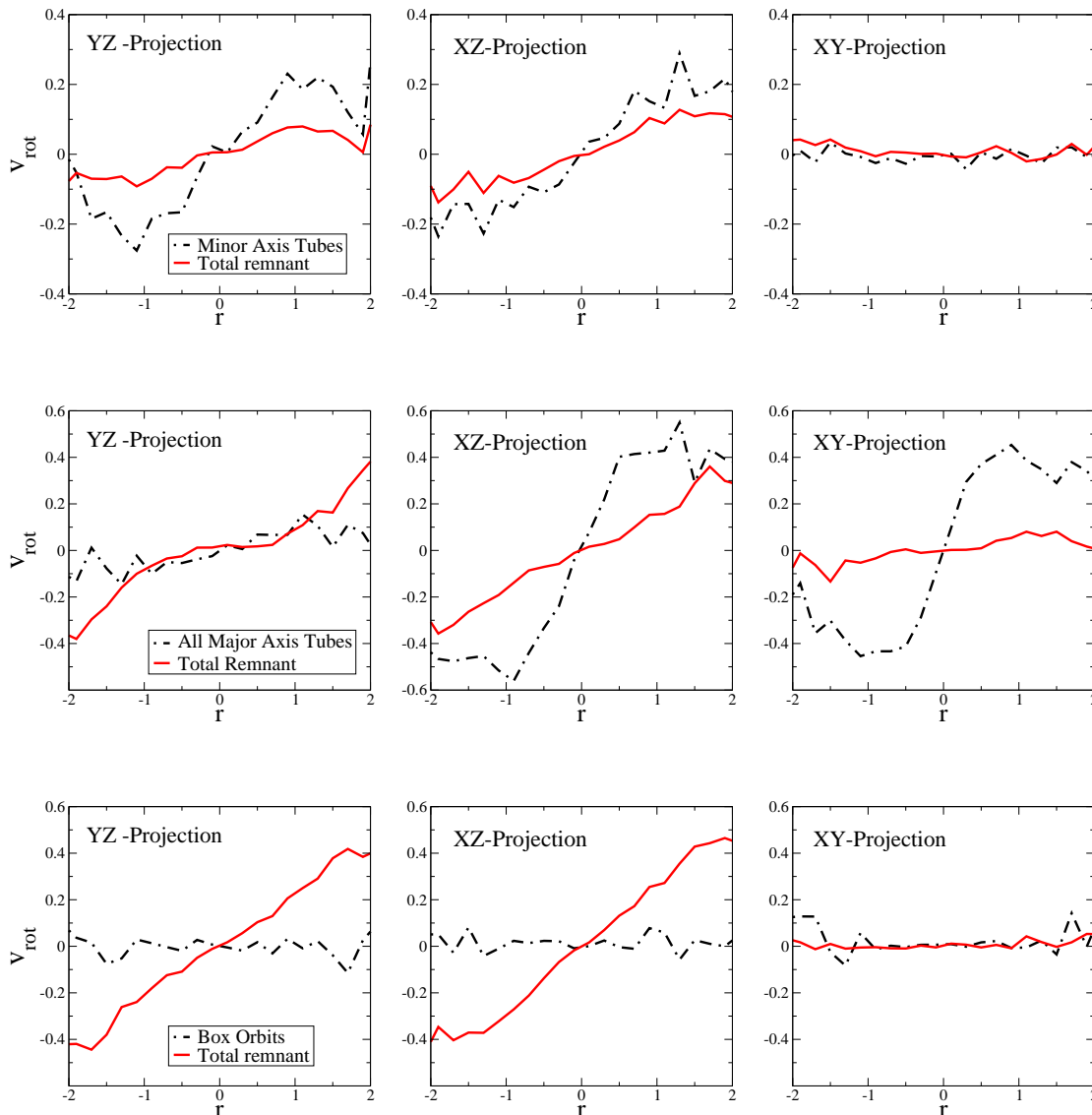


Figure 15. Comparison of the rotational properties of single orbit classes (dot-dashed lines) with the rotation of the whole remnant (solid lines). Three characteristic remnants, two 1:1 and one 3:1, are chosen. In each case an orbit class is extracted and projected along the major, intermediate and short axis (YZ, XZ, XY-plane). The observational slit is positioned along the apparent major axis. **Top Row:** Minor axis tubes in a 1:1 remnant. They show rotation in the YZ and XZ projection and no rotation in the XY projection. **Middle Row:** Major axis tubes (both types) in a prolate 1:1 remnant. Strong rotation is present in the XZ and the XY projection and almost non in the YZ projection. **Bottom Row:** Box orbits in a 3:1 remnant. They show no rotation in any projection as expected, however the whole remnant does rotate strongly.

7.3.2 Global Correlations

It is known that the LOSVDs of early-type galaxies can deviate significantly from pure Gaussian profiles. The two most important parameters are the third order coefficient of the Gauss-Hermite expansion, h_3 , which measures the asymmetric deviations and the fourth order coefficient h_4 which measures the symmetric deviations from a Gaussian profile. We follow the definition of Bender, Saglia, & Gerhard (1994) in calculating the effective parameters, termed $h_{3\text{eff}}$ and $h_{4\text{eff}}$ by averaging from the center of the remnant to $0.75 r_{\text{eff}}$. They found correlations between $h_{3\text{eff}}$ and (v/σ)

as indicated in Fig.16. The merger remnants cannot reproduce this correlation. It is apparent that the values scatter around zero for $h_{3\text{eff}}$ and are not as negative as expected from observations for a given v/σ . The picture changes if the same analysis is done taking only particles on minor axis tubes. Much more negative $h_{3\text{eff}}$ can be reached. The measured values for the 1:1 and the 2:1 remnants even fall on the observed relation, the 3:1 and 4:1, however, do not. While the merging process is sufficiently violent to introduce asymmetries in the LOSVD in the 1:1 and 2:1 remnants, it is not so in the 3:1 and 4:1 remnants. The problem remains that the $h_{3\text{eff}}$ is too positive for the *total* merger

remnant. One must assume that the other orbit classes have an impact, too. This is hinted at in Fig.17, left panel. We see that merger remnants with positive h_3 values tend to have a dominant box orbit population and we do not find a single box-dominated remnant with a negative $h_{3\text{eff}}$. Even some tube-dominated subsamples, like the 4:1 mergers, show a tight correlation of $h_{3\text{eff}}$ with the box to minor axis tube ratio. The situation for $h_{4\text{eff}}$ is not as clear. Although some correlation can be seen for very box rich remnants, there is no evidence for this in 3:1 and 4:1 remnants. $h_{4\text{eff}}$ is positive in all remnants.

7.3.3 Local Correlations

In addition to observed correlations for the effective h_3 there also exist local correlations within a single galaxy. As expected from a rotating axisymmetric system the rotation velocity is anti-correlated with h_3 and has opposite sign (Bender, Saglia, & Gerhard 1994; Halliday et al. 2001; Pinkney et al. 2003). This anti-correlation is violated in most collisionless merger remnants (Bendo & Barnes 2000, Naab & Burkert 2001) and poses a serious problem for the merger hypothesis. Decomposing the merger remnant into orbital components is an ideal tool to shed light on this question. Fig. 18 shows a 3:1 merger remnant, observed along the true major axis. The h_3 and v_{rot} for the total remnant are anti-correlated in the outer parts, but correlated in the center (Fig. 18, right side). Exactly the same procedure is done with the particles classified as minor axis tubes. This time an anti-correlation is seen over the whole radial range. It is only when we superpose the box orbits that the kinematics starts to resemble closely the kinematics of the whole remnant. We find that the minor axis tube components of *all* merger remnants display the observationally predicted h_3 - v_{rot} anti-correlation. One could conclude that there can not exist a sizeable box orbit population in the center of real elliptical galaxies. But probably the situation is more complicated in real galaxies, e.g. if a central disk component is present (Naab & Burkert 2001). Also in our 1:1 remnants the sometimes strong major axis tube component can complicate the effect of superpositions considerably.

8 SUMMARY AND CONCLUSIONS

We have presented a detailed analysis of the orbital content of a statistical sample of collisionless merger remnants with mass ratios of 1:1, 2:1, 3:1, and 4:1 using the spectral method of CA98. The orbital content has been tested to remain constant over at least a few dynamical times at the half mass radius. For the 1:1 sample we have repeated the analysis with remnants of bulgeless progenitor disks and remnants of mergers with a larger pericenter distance. We have investigated in detail the relation between the orbital content of the merger remnants without figure rotation and their projected kinematic and photometric properties. For remnants with bulges minor axis tubes and box orbits are the dominant orbit class, independent of the mass ratio. Only for remnants of bulgeless disks, boxlets and box orbits dominate the systems. On average the fraction of minor axis tubes doubles from a mass ratio of 1:1 to 4:1 whereas the fraction of box orbits decreases weakly. The minor axis tube

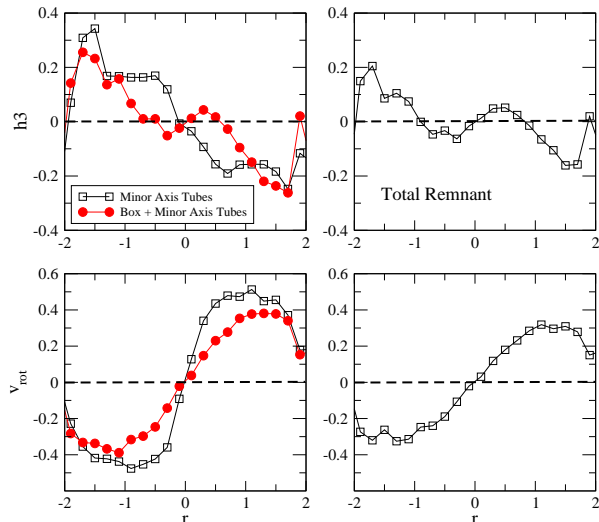


Figure 18. Left: h_3 (top) and v_{rot} (bottom) for a 3:1 remnant taken along the major axis for minor axis tubes and minor axis tubes and box orbits superposed. While for the minor axis tubes the signs of h_3 and v_{rot} are anti-correlated, a correlated inner ridge forms in h_3 when the box orbits are added. Right: Like before, but for the total remnant

orbits predominantly originate from the progenitor disks. In contrast equal numbers of box orbits stem from the disk and the bulge of the progenitor galaxies. The triaxiality of the remnants correlates with the orbital content. The minor axis tube fraction strongly decreases from oblate to prolate systems while the remnants with the highest box orbit fraction are the most triaxial ones. This is in agreement with analytical predictions for self consistent triaxial systems (Statler 1987).

Interestingly, the division line defined by observers between pressure supported and rotation supported systems of $(v/\sigma)^* = 0.7$ coincides with a box to minor axis tube ratio of unity. Pressure supported systems have more box than minor axis tube orbits, minor axis tubes prevail in rotation supported systems. Strong minor axis rotation can, as expected, only be found in remnants with a significant number of major axis tube orbits. The projected central velocity dispersion of the remnants is not only connected to their mass but also to their balance of box to minor axis tube orbits.

The observed anti-correlation between the asymmetry of the LOSVD measured by h_3 and the ratio of v/σ found in early-type galaxies by Bender, Saglia, & Gerhard (1994) can not be reproduced by collisionless merger remnants. We do find some remnants with negative $h_{3\text{eff}}$ but with an amplitude that is a factor of five too small compared to observations. All remnants with more box than minor axis tubes show a positive $h_{3\text{eff}}$. The observed correlation can be better reproduced if we consider only particles on minor axis tubes. Therefore we conclude that any additional physical process during the merging of the galaxies that would reduce the number of box orbits and increase the number of tube orbits would naturally lead to the observed correlation. The most likely process is the destruction of box orbits by a large mass concentration at the center of the

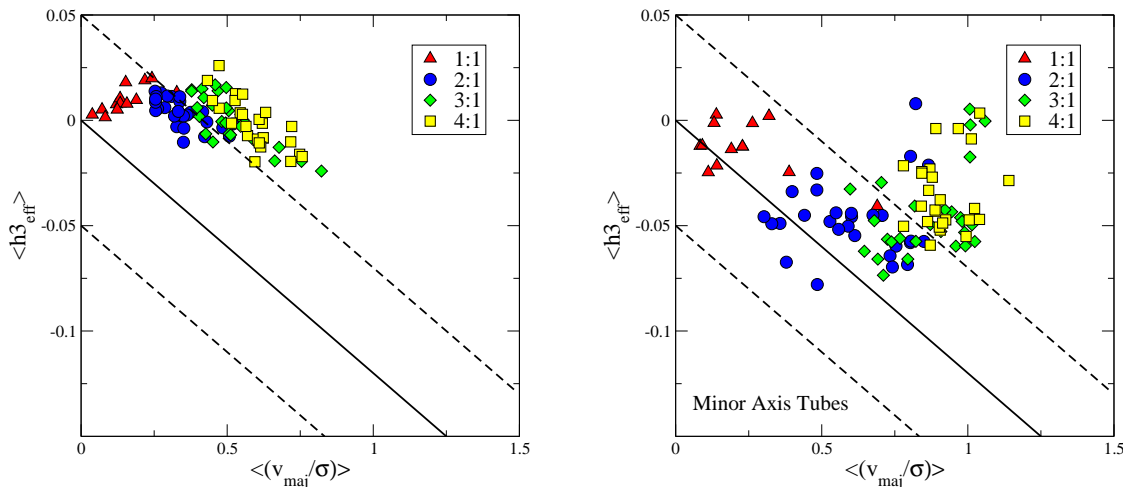


Figure 16. The ratios of rotation along the apparent major axis and central velocity dispersion as function of the effective h_3 parameter are shown for simulated merger remnants and compared with observed galaxies as reported by Bender, Saglia, & Gerhard (1994). The observed correlations are indicated by solid lines, the observational spread by dashed lines. **Left:** Measurements for the total remnant, each remnant is averaged over 50 projections. The values are far too positive **Right:** Only minor axis tubes, also averaged over 50 projections. The minor axis tube components of 1:1 and 2:1 merger remnants agree well, at least kinematically, with observations. 3:1 and 4:1 mergers also have more negative values, but not enough to explain the observational data.

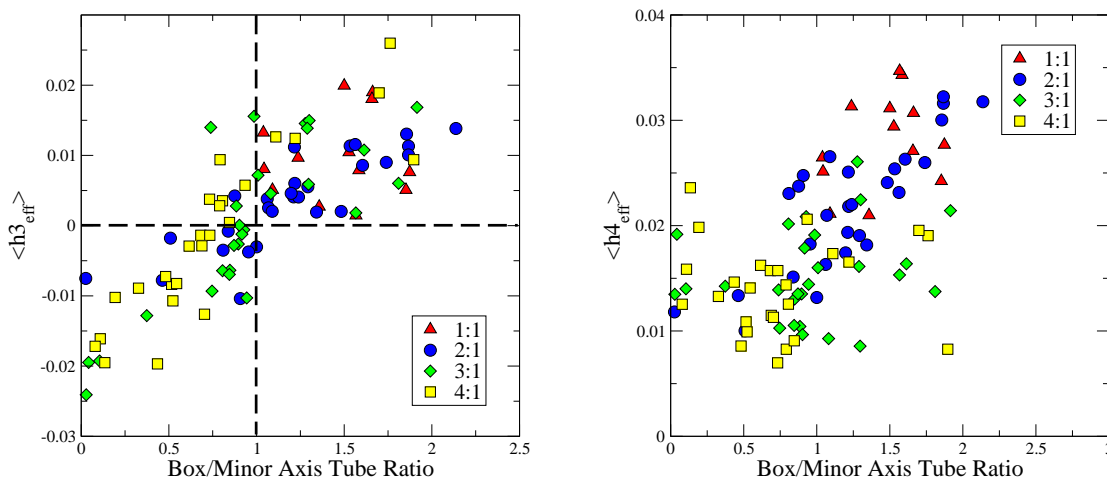


Figure 17. Left: Relation between the box to minor axis tube ratio and $h_{3\text{eff}}$. The horizontal line divides positive and negative values for h_3 and the vertical line minor axis tube from box orbit dominated remnants. Box orbit dominated remnants tend to have positive $h_{3\text{eff}}$. **Right:** Relation between the box to minor axis tube ratio and $h_{4\text{eff}}$

galaxies (Lees & Schwarzschild 1992). Those mass concentrations can arise from infalling gas during a merger of gas rich disks (Barnes & Hernquist 1996). Alternatively a very concentrated bulge could have a similar effect.

Merger remnants which are dominated by minor axis tube orbits have predominantly disky projections. However, they can appear boxy for certain projections. It is only possible to produce a pure boxy remnant when the majority of particles move on box orbits. This might provide a fundamental limitation for the applicability of axisymmetric Schwarzschild modeling of the most massive, probably tri-

axial, elliptical galaxies (Cretton, Rix, & de Zeeuw 2000). These models can only reproduce boxy isophotal shapes with tube orbits; our models predict that those galaxies will on average have disky projections.

ACKNOWLEDGMENTS

We are grateful to Daniel Carpintero and Luis Aguilar for making available their classification code and to Shunsuke Hozumi for making available his self consistent field

code. We thank Ralf Bender, James Binney, Hans-Walter Rix for helpful discussions and comments. Roland Jesseit acknowledges financial support by the SFB 375 Astro-Teilchenphysik of the DFG.

REFERENCES

- Alam, S. M. K. & Ryden, B. S. 2002, *ApJ*, 570, 610
 Burkert, A. & Naab, T. 2004, in *Galaxies and Chaos*, eds G. Contopoulos & N. Voglis (Springer), p. 327
 Arnold, R., de Zeeuw, P. T., & Hunter, C. 1994, *MNRAS*, 271, 924
 Barnes, J. E. 1992, *ApJ*, 393, 484
 Barnes, J. E. 1998, *Saas-Fee Advanced Course 26: Galaxies: Interactions and Induced Star Formation*, 275
 Barnes, J. E. & Hernquist, L. 1996, *ApJ*, 471, 115
 Bender, R. 1988, *A&A*, 193, L7
 Bender, R., Döbereiner, S., & Möllenhoff, C. 1988, *A&AS*, 74, 385
 Bender, R., Saglia, R. P., & Gerhard, O. E. 1994, *MNRAS*, 269, 785
 Bender, R., Surma, P., Doebereiner, S., Moellenhoff, C., & Madejsky, R. 1989, *A&A*, 217, 35
 Bendo, G. J. & Barnes, J. E. 2000, *MNRAS*, 316, 315
 Binney, J. 1978, *MNRAS*, 183, 501
 Binney, J. 1985, *MNRAS*, 212, 767
 Binney, J. & Spergel, D. 1982, *ApJ*, 252, 308
 Carpintero, D. D. and Aguilar, L. A., 1998, *MNRAS*, 298, 1
 Cretton, N., Naab, T., Rix, H., & Burkert, A. 2001, *ApJ*, 554, 291
 Cretton, N., Rix, H., & de Zeeuw, P. T. 2000, *ApJ*, 536, 319
 Clutton-Brock, M. 1973, *Ap&SS*, 23, 55
 Davies, R. L., Efstathiou, G., Fall, S. M., Illingworth, G., & Schechter, P. L. 1983, *ApJ*, 266, 41
 Faber, S. M. & Jackson, R. E. 1976, *ApJ*, 204, 668
 Franx, M. 1988, *MNRAS*, 231, 285
 Franx, M., Illingworth, G., & de Zeeuw, T. 1991, *ApJ*, 383, 112
 Hairer, E., Nørsett S. P. and Wanner, G. 1993, *Solving Ordinary Differential Equations. Nonstiff Problems*. Springer Series in Comput. Math., vol. 8.
 Halliday, C., Davies, R. L., Kuntschner, H., Birkinshaw, M., Bender, R., Saglia, R. P., & Bagglely, G. 2001, *MNRAS*, 326, 473
 Hernquist, L. & Ostriker, J. P. 1992, *ApJ*, 386, 375
 Hernquist, L. 1990, *ApJ*, 356, 359
 Hernquist, L. 1992, *ApJ*, 400, 460
 Hernquist, L. 1993, *ApJ*, 409, 548
 Heyl, J. S., Hernquist, L., & Spergel, D. N. 1994, *ApJ*, 427, 165
 Heyl, J. S., Hernquist, L., & Spergel, D. N. 1995, *ApJ*, 448, 64
 Heyl, J. S., Hernquist, L., & Spergel, D. N. 1996, *ApJ*, 463, 69
 Hozumi, S. 1997, *ApJ*, 487, 617
 Hozumi, S. & Hernquist, L. 1995, *ApJ*, 440, 60
 Kawai, A., Fukushige, T., Makino, J., & Taiji, M. 2000, *PASJ*, 52, 659
 Laskar, J. 1993, *Physica D Nonlinear Phenomena*, 67, 257
 Lees, J. F. & Schwarzschild, M. 1992, *ApJ*, 384, 491
 Naab, T. & Burkert, A. 2001, *ApJL*, 555, L91
 Naab, T. & Burkert, A. 2003, *ApJ*, 597, 893
 Naab, T., Burkert, A., & Hernquist, L. 1999, *ApJL*, 523, L133
 Nieto, J.-L., Capaccioli, M., & Held, E. V. 1988, *A&A*, 195, L1
 Papaphilippou, Y., & Laskar, J. 1996, *A&A*, 307, 427
 Papaphilippou, Y., & Laskar, J. 1998, *A&A*, 329, 451
 Pfenniger, D. & Friedli, D. 1991, *A&A*, 252, 75
 Pierce M. J., Tully R. B., 1992, *ApJ*, 387, 47
 Pinkney, J., et al. 2003, *ApJ*, 596, 903 J
 Rix, H., de Zeeuw, P. T., Cretton, N., van der Marel, R. P., & Carollo, C. M. 1997, *ApJ*, 488, 702
 Scorza, C. & Bender, R. 1995, *A&A*, 293, 20
 Schwarzschild, M. 1979, *ApJ*, 232, 236
 Schwarzschild, M., 1993, *ApJ*, 409, 563
 Statler, T. S. 1987, *ApJ*, 321, 113
 Statler, T. S., Emsellem, E., Peletier, R. F., & Bacon, R. 2004, *MNRAS*, 353, 1
 Toomre, A. & Toomre, J. 1972, *ApJ*, 178, 623
 Wagner, S. J., Bender, R., & Moellenhoff, C. 1988, *A&A*, 195, L5
 Weil, M. L. & Hernquist, L. 1996, *ApJ*, 460, 101